Sensors & Diagnostics

PAPER

View Article Online
View Journal | View Issue

Check for updates

Cite this: *Sens. Diagn.*, 2026, **5**, 705

Unlocking the potential of proton-mediated detection of ascorbic acid with a Ni–Co bimetallic MOF based extended gate FET

Guru Prasad Kuppuswamy,†[ab] Akshaya Vinukumar,†[a] Kishore Pushparaj,[c] Sujitha Murugaiyan,[c] Larisa Lvova, *[d] Surya Velappa Jayaraman, [ef] Corrado Di Natale *[ch] and Yuvaraj Sivalingam *[eg]

Received 2nd December 2025,
Accepted 11th February 2026

DOI: 10.1039/d5sd00217f

rsc.li/sensors

The possibility to quantify ascorbic acid (AA) using a Ni–Co MOF-coated carbon paper electrode within an extended gate FET setup (EGFET), operated at zero gate potential (open-circuit potential, OCP), has been investigated. Under these conditions, the Ni–Co MOF/CP electrode outperformed the single metal-based Ni-MOF and Co-MOF, demonstrating a wide detection range from 454 nM to 224.9 μM, encompassing both low and high AA levels in human blood, and a response time under 7 seconds. The sensor has shown a pronounced selective response to AA in the presence of several potential interferents such as glucose, sucrose, nicotine, lactose, and fructose. The sensitivity of the Ni–Co MOF/CP sensor to AA was estimated as 6.5284 nA μM^{-1} cm^{-2}, with a limit of detection (LOD) of 45.1 nM and a limit of quantification (LOQ) of 136 nM. These findings indicate the potential and suitability of the Ni–Co MOF/CP electrode for detecting ascorbic acid in human blood serum. A key novelty of this work is the use of OCP to detect AA with Ni–Co MOF/CP, leveraging proton conduction *via* a combined Grotthuss and vehicular mechanism.

1. Introduction

In contemporary times, individuals are confronted with a multitude of unfamiliar ailments, posing a significant difficulty for medical professionals in identifying their underlying causes and developing appropriate treatments. Nowadays, one of the forms of dietary insufficiency that persists is known as scurvy, whose primary cause is the absence of immunity and inadequate adherence to the recommended dietary allowance (RDA), and in particular, low uptake of vitamin C or ascorbic acid (AA). The global morbidity data for scurvy reveal a significant prevalence 1among individuals residing in lower socioeconomic areas with limited access to the RDA, and sporadically appearing in global health epidemics today. Alcoholics and institutionalised communities are particularly vulnerable to this deficit. The insufficiency of vitamin C is observed even in industrialised populations that have been inadequately fortified with the RDA.[1–4] The well-known antioxidant properties of AA are crucial in mitigating oxidative stress and facilitating collagen formation. While left untreated, scurvy can become a lethal disease. Due to evolutionary genetic mutations, humans and other primates have lost the ability to produce AA, and the consumption of AA by humans can only be achieved through external means. AA is most effectively obtained from plant-based meals. The diet commonly consists of fruits, vegetables, and whole grains, which are known for their high fibre content and low levels of fat and cholesterol. The gastrointestinal tract absorbs around 80–90% of AA, which thereafter circulates in plasma, leukocytes, and red blood cells, ultimately entering all tissues.[5] The pituitary and adrenal glands, leukocytes, brain, ocular tissues, and fluids exhibit elevated concentrations of vitamin C.

The normal concentration of AA in humans lies in the range of 36.1–79.4 μmol l^{-1} in blood, with the typical medium concentration of AA in plasma of 50 μM l^{-1}.[6] The excessive intake of AA has been associated with several adverse effects, including diarrhoea, nausea, vomiting, heartburn, abdominal bloating, cramps, headache, sleeplessness, and the formation of kidney stones. According to depletion-repletion tests

[a] *Department of Physics and Nanotechnology, SRM Institute of Science and Technology, Kattankulathur 603203, Tamil Nadu, India*
[b] *Department of Materials Engineering, Ben-Gurion University of the Negev, Beer-Sheva, 84105, Israel*
[c] *Department of Electronic Engineering, University of Rome Tor Vergata, Via del Politecnico 1, 00133 Roma, Italy. E-mail: dinatale@uniroma2.it*
[d] *Department of Chemical Science and Technologies, University of Tor Vergata, Via della Ricerca Scientifica, 000133 Rome, Italy. E-mail: Larisa.Lvova@uniroma2.it*
[e] *Centre for Advanced Translational Research, KPR College of Arts, Science and Research, Coimbatore 641407, Tamil Nadu, India. E-mail: yuvaraj.s@kprcas.ac.in*
[f] *New Industry Creation Hatchery Center (NICHe), Tohoku University, Aoba-ku, Sendai 980-8579, Miyagi, Japan*
[g] *Department of Electronics and Communication Engineering, Bannari Amman Institute of Technology, Sathyamangalam 638401, Tamil Nadu, India*
[h] *Centre for Interdisciplinary Research (CIDR), SRM University-AP, Amaravati, Andhra Pradesh, 522502, India*
† Both the authors have contributed equally

Open Access Article. Published on 20 February 2026. Downloaded on 5/25/2026 6:49:37 PM.
This article is licensed under a Creative Commons Attribution-NonCommercial 3.0 Unported Licence.

Open Access Article. Published on 20 February 2026. Downloaded on 5/25/2026 6:49:37 PM. This article is licensed under a Creative Commons Attribution-NonCommercial 3.0 Unported Licence.

conducted by the National Institutes of Health (NIH), fatigue was observed when the concentrations of AA in plasma were below around 20 μM.[6] Significantly, a shortage in vitamin C results in the body's inability to effectively combat free radicals, hence causing damage to cells and tissues, giving rise to scurvy conditions, when the decrease of AA plasma concentration level decreases below 11 μM l^{-1}.[6] However, typical physical signs appear generally at a much lower level, such as 3–5 μM.[6]

Several approaches have been published for the determination of AA. These techniques include the typical titrimetric method, fluorimetry, spectrometry, chemiluminescence, enzymatic methods, capillary electrophoresis, electrochemical methods, amperometry methods, and HPLC.[7] Among these available techniques, the electrochemical method is widely regarded as a more efficient and feasible approach due to its advantages in terms of time efficiency, cost-effectiveness, and highly sensitive detection. Currently, FET-based biosensors have garnered significant interest from the scientific community due to their unique characteristics, including high sensitivity, cost-effectiveness, low power consumption, and convenient integration for portability.

The EGFET safeguards the FET structure from the chemical environment, allowing only the sensing membrane to come into contact with the electrolyte. The sensing membrane can be reused several times, provided that the membrane exhibits reproducibility. Moreover, these characteristics can enhance the utilisation of the EGFET for single-use electrode type. In general, the EGFET exhibits enduring stability due to the absence of interactions between the ions in the chemical solution and the gate insulator. The extended gate field-effect transistor (EGFET) consists of two primary components: the extended electrode, which incorporates the sensing membrane, and the traditional metal oxide semiconductor field effect transistor (MOSFET).[8] The operation of an EGFET involves an extended gate terminal that is connected to the working electrode, while the reference electrode is used to bias the gate.

Metal–organic frameworks (MOFs) have garnered considerable interest in recent decades due to their notable characteristics, including high specific surface areas, large pore volumes, and well-defined pore size distribution. Additionally, MOFs are recognised for their chemical stability, mechanical strength, and structural diversity, making them highly promising for applications in biosensing. A highly organised infinite network is formed by the connection of metal ions or ion clusters with organic ligands by coordination bonds, supplemental hydrogen bonds, metallic bonding, or Van der Waals force contact. In contrast to conventional porous materials, metal–organic frameworks (MOFs) provide several notable benefits, including a wide range of scaffold structures, adjustable pore sizes, and a substantial number of active sites.[9] The utilisation of metal–organic frameworks (MOFs) as precursors for the synthesis of novel materials is seeing significant advancements due to the diverse compositional and structural characteristics they offer. The wide range of characteristics offers fresh possibilities for effectively combining MOF materials with other compounds and adjusting the components to achieve specific capabilities. Furthermore, the utilisation of long-range ordering at a molecular level has been shown to make MOFs a valuable precursor.[10] MOFs have found extensive applications in several fields such as biomolecule detection, catalysis, electrochemical energy storage and conversion, biological and medical applications and many more, as documented in the literature.[11] Few instances of MOF-based sensors include the use of Ca-MOF, Zn-MOF/GO, and GA-UiO-66-NH_2 for the detection of Hg^{2+}, As^{3+}, and Pb^{2+}, respectively.[12–14] Extending these principles to biomedical applications, Lee *et al.* recently introduced a rapid extended-gate field-effect transistor (R-EGFET)-based biosensor incorporating an HPIV aptamer and UiO-66 metal–organic framework (MOF) nanoparticles, enabling rapid and specific detection of human parainfluenza virus (HPIV).[15]

In this study, the influence of Ni–Co MOF/CP catalyst loading on the proton-mediated electrochemical detection of AA, with the EGFET sensor under open circuit potential (OCP) conditions, has been investigated. Conventional three-electrode amperometric sensors often require an external applied potential, which can trigger unwanted redox reactions from co-existing electroactive species in complex biological samples, leading to significant interference, electrode fouling, and reduced reliability for *in vitro* or *in vivo* analysis.[16] In contrast, our open-circuit potential (OCP) sensor, based on the proton-conducting Ni–Co MOF/CP composite, operates passively with negligible current draw (nA range after stabilization), minimizing power consumption. By maintaining the electrode at its low equilibrium OCP value without external bias, it suppresses unintended oxidation/reduction of interferents, thereby enhancing selectivity. The design is simple and reproducible —requiring only replacement of a single working electrode— while the system is self-powered by ascorbic acid oxidation in biological fluids releasing protons that drive the OCP response *via* Grotthuss and vehicular mechanisms, eliminating external energy needs and enabling potential miniaturization. SKP was used to study the surface of electrodes with and without AA to under the sensing behaviours. The developed Ni–Co MOF/CP EGFET has demonstrated a wide working range from 454 nM to 224.9 μM, a short response time (less than 7 seconds), and enhanced selectivity towards AA in the presence of several potential interferents present in blood, thus demonstrating the potential applicability for clinical applications.

2. Experimental section

2.1. Chemicals and materials

L-ascorbic acid [AA ($C_6H_8O_6$)], dextrose [Glu ($C_6H_{12}O_6$)], sucrose [Suc ($C_{12}H_{22}O_{11}$)], fructose [Fru ($C_6H_{12}O_6$)], uric acid [UA ($C_5H_4N_4O_3$)], 10× phosphate buffer saline (PBS), nickel(II)

© 2026 The Author(s). Published by the Royal Society of Chemistry

Open Access Article. Published on 20 February 2026. Downloaded on 5/25/2026 6:49:37 PM. This article is licensed under a Creative Commons Attribution-NonCommercial 3.0 Unported Licence.

nitrate hexahydrate [$Ni(NO_3)_2{\cdot}6H_2O$], cobalt nitrate hexahydrate ($Co(NO_3)_2{\cdot}6H_2O$), potassium chloride (KCl), Nafion 117 solution (5%), 1,3,5-benzenetricarboxylic acid [BTC ($C_9H_6O_6$)], polyvinylpyrrolidone (PVP) K30 [$(C_6H_9NO)_x$], isopropyl alcohol (IPA, 99%) and *N*,*N*-dimethylformamide [(DMF), C_3H_7NO] were obtained from Sisco Research Laboratories Pvt. Ltd., India. Premium grade ethanol 100% was obtained from Hayman Group Ltd. Commercial carbon paper (CP) was obtained from Sainergy Fuel Cell India Pvt. Ltd. Deionised (DI) water was used throughout the experiment. The MOSFET employed in this study is an n-type MOSFET (TN2540N8-G) from Microchip Technology, Thailand Co., Ltd.

The experiments involving human blood serum were performed in accordance with the Guidelines in India and approved by the ethics committee at the SRM Institute of Science and Technology (Deemed to be University). The blood sample used in this study was voluntarily provided by one of the authors with informed consent.

2.2. Apparatus

Bruker USA D8 Advance and Davinci X-ray diffractometers were used for X-ray measurements. High-resolution scanning electron microscope (HRSEM) and Brunauer–Emmett–Teller (BET) measurements were performed using a Thermo Scientific Apreo S and a Quantachrome Instruments Autosorb IQ series, respectively. An XPS PHI Versaprobe III was used to perform X-ray photoelectron spectroscopy (XPS) studies. Work function and contact potential difference measurements were investigated utilising a scanning Kelvin probe [SKP5050 (KP Technology, UK)] with a SPV020 module. The dynamic/transient study (I_D vs t) was carried out using a Keithley semiconductor parameter analyser (4200A-SCS) equipped with a source measure unit (SMU).

For *I*–*t* measurements, the prepared electrode was firmly fixed using an electrode holder with a copper contact. The reference electrode used in this investigation was Ag/AgCl (saturated KCl), and the electrolyte solution was 1× PBS (prepared by diluting 10× PBS). A constant distance of 1 cm was maintained between the prepared working electrode and the reference electrode. Only the coated section of the electrode was exposed to the electrolyte (PBS), while everything else was covered with Teflon tape. An n-type surface-mount MOSFET (TN2540N8-G) was soldered to a printed circuit board (PCB) for the ascorbic acid detection experiment. Fig. 1 shows the schematic representation of the experimental setup.

2.3. Synthesis procedure

2.3.1. Synthesis of Ni–Co MOF. The synthesis of Ni–Co MOF was adapted from the previously reported literature.[9] In detail, 0.432 g $Ni(NO_3)_2{\cdot}6H_2O$, 0.432 g $Co(NO_3)_2{\cdot}6H_2O$, 0.3 g 1,3,5-benzene tricarboxylic acid, and 3 g PVP were dissolved in a 60 mL mixture solution with the volume ratio of distilled water : ethanol : DMF = 1 : 1 : 1 at room temperature under supersonic vibration for 30 min followed by stirring of 15 min. The mixture solution was then transferred into a 100 mL Teflon-line autoclave and kept at 150 °C for 10 h. Thereafter, the pale purple colored product was collected through centrifugation by washing with ethanol and DI. The obtained precipitate was dried in a hot air oven at 80 °C overnight.

2.3.2. Synthesis of Ni MOF and Co MOF. The typical synthesis of Ni MOF and Co MOF was taken from the reported literature.[17] 0.864 g $Ni(NO_3)_2{\cdot}6H_2O$, 0.864 g $Co(NO_3)_2{\cdot}6H_2O$, 0.3 g 1,3,5-benzene tricarboxylic acid, and 3 g PVP were dissolved in 60 mL mixture solution with the volume ratio of distilled water : ethanol : DMF = 1 : 1 : 1 at room temperature under stirring for 30 min and after sonication for 15 min. The mixture solution was then transferred into a 100 mL Teflon-line autoclave and kept at 150 °C for 10 h. Thereafter, the pale green and dark purple products were collected through centrifugation by washing

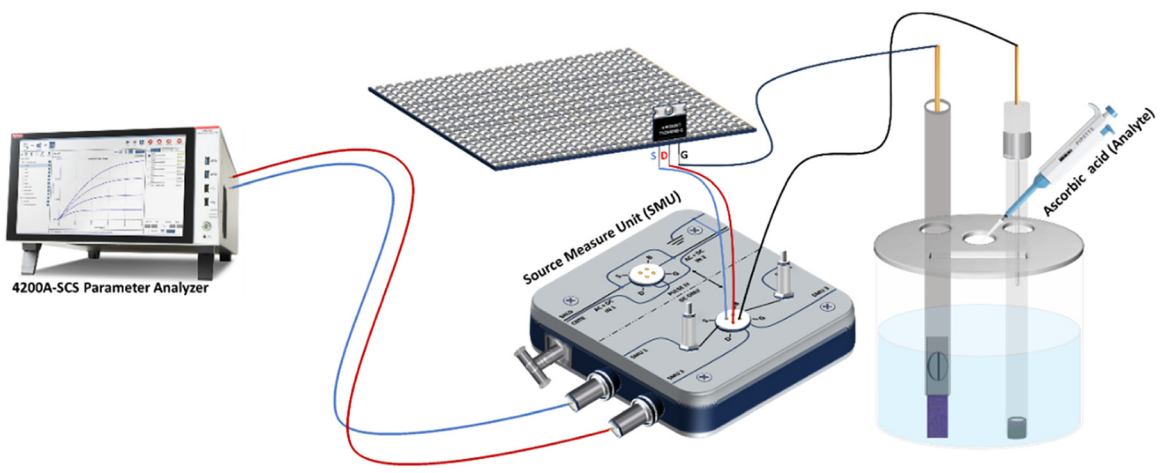

Fig. 1 Schematic representation of the EGFET-based experimental setup.

Open Access Article. Published on 20 February 2026. Downloaded on 5/25/2026 6:49:37 PM.
This article is licensed under a Creative Commons Attribution-NonCommercial 3.0 Unported Licence.

with ethanol and DI. The obtained precipitate was dried in hot air oven at 80 °C overnight.

2.4. Electrode preparation

Carbon paper was washed with DI, ethanol, and IPA under sonication in order to get rid of the impurities. Then, the pre-treated carbon paper was dried at 80 °C and stored in an air-tight container. 1 mg of Ni–Co MOF sonicated in a mixture of 500 μl of DI water, 500 μl of ethanol and 10 μl of 1% Nafion (diluted 5% Nafion with isopropyl alcohol and DI water) for 15 min. Following that, several weight loadings of Ni–Co MOF ink solution were made and dropcasted onto the CP, spanning an area of 0.5 × 0.5 cm^2, in order to select the optimal ink solution for the whole experiment. The accuracy of AA assessment with the developed electrodes was estimated through limit of detection (LOD) and limit of quantification (LOQ) estimation.

3. Results and discussion

3.1. Material characterisation

The XRD spectra as shown in Fig. 2a reveal the pattern of Ni MOF, Co MOF and Ni–Co MOF. Here, these three patterns have shown the common planes of (012) and (110) in the peak position at ~9° and ~12°, respectively. By analysing the XRD pattern, we can clearly see that the peak positions of the Ni MOF and Ni–Co MOF compositions are very comparable, in which the crystal planes (220) and (913) belonging to the Ni MOF also appear in the Ni–Co MOF. This phenomenon occurs because a significant portion of Co^{2+} ions is replaced by Ni^{2+} ions during the synthesis of the Ni–Co MOF. Furthermore, the degree of crystallinity of the Ni–Co MOF is weaker compared to the monometallic Ni MOF and Co MOF. The possible reason for the low crystallinity of Ni–Co MOF could be due to the presence of the Co MOF, which could have suppressed its crystallinity.[18–23]

Fig. 2b shows the FTIR spectra of Ni MOF, Co MOF and Ni–Co MOF. The peak at ~745.90 corresponds to the bending of the C–H bond in an out-of-plane motion. This band provides evidence of its association with the 1,3,5-benzene-tri-carboxylic acid (BTC) structure. The C–H bending (out-of-plane) vibration is employed to determine the position of substituents on the aromatic ring. Based on the shape of the peak, one may obviously determine if the aromatic ring belongs to mono-, di-, tri-, tetra-, penta-, or hexa-substituted compounds. For the ~1110.65 –C–O stretching vibration, its absorption is always coupled with the C–C band. The raised band at the 1110.65 cm^{-1} position helps to assign the primary, secondary, and tertiary structure in alcohols or to identify the presence of phenol compounds. The intense peak at ~1373.97 corresponds to the CH_3 bending vibration. The CH_3 group has mainly appeared due to the DMF used during the synthesis of MOF. Interestingly, methyl groups are unable to form hydrogen bonds and will not interact with polar compounds such as water. Thereby, the material will remain stable over the long-term exposure to aqueous-based electrolytes. The ~1442.62 band corresponds to the C–O–H bending vibration. This band is hard to recognize because it overlaps with the position of the CH_3 bending vibration, which is a sharp and dominant band. As a result, the C–O–H band appears unclear. On the other hand, the band at ~1623.98 signifies the C=C stretching vibration, which belongs to an aromatic compound. This band always accompanies a less intense peak, which appears around ~1550–1450 cm^{-1}.[24]

HRSEM images of Ni MOF, Co MOF and Ni–Co MOF are shown in Fig. 3. Fig. 3a shows the Ni MOF, which looks like a cluster made of nanorods. On the other hand, the Co-MOF looks like nanocrystal blocks as shown in Fig. 3c. Meanwhile, the composite Ni–Co-MOF has formed into a spherical structure with an average particle size of 6.1 ± 1.7 μm, as displayed in Fig. 3c. Further investigation at lower magnification shows the spherical balls with a more uniform surface as seen in Fig. 3d. Fig. 3e reveals that the Ni Co-MOF spheres are made of nanorod like structures and measure 128 ± 32 nm in width, and the length of the rods is observed to be irregular. When compared to Co MOF, the nickel occupation is higher, which is confirmed through EDX spectra as shown in Fig. S1. As a result, we can see in the XRD that the position of the plane formed in Ni MOF

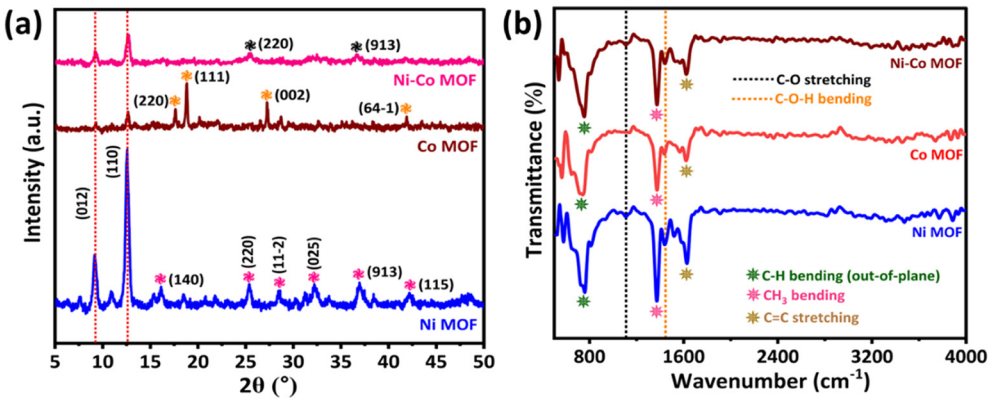

Fig. 2 (a) XRD spectra of Ni MOF, Co MOF and Ni–Co MOF and (b) FTIR spectra of Ni MOF, Co MOF and Ni–Co MOF.

© 2026 The Author(s). Published by the Royal Society of Chemistry

Open Access Article. Published on 20 February 2026. Downloaded on 5/25/2026 6:49:37 PM.
This article is licensed under a Creative Commons Attribution-NonCommercial 3.0 Unported Licence.

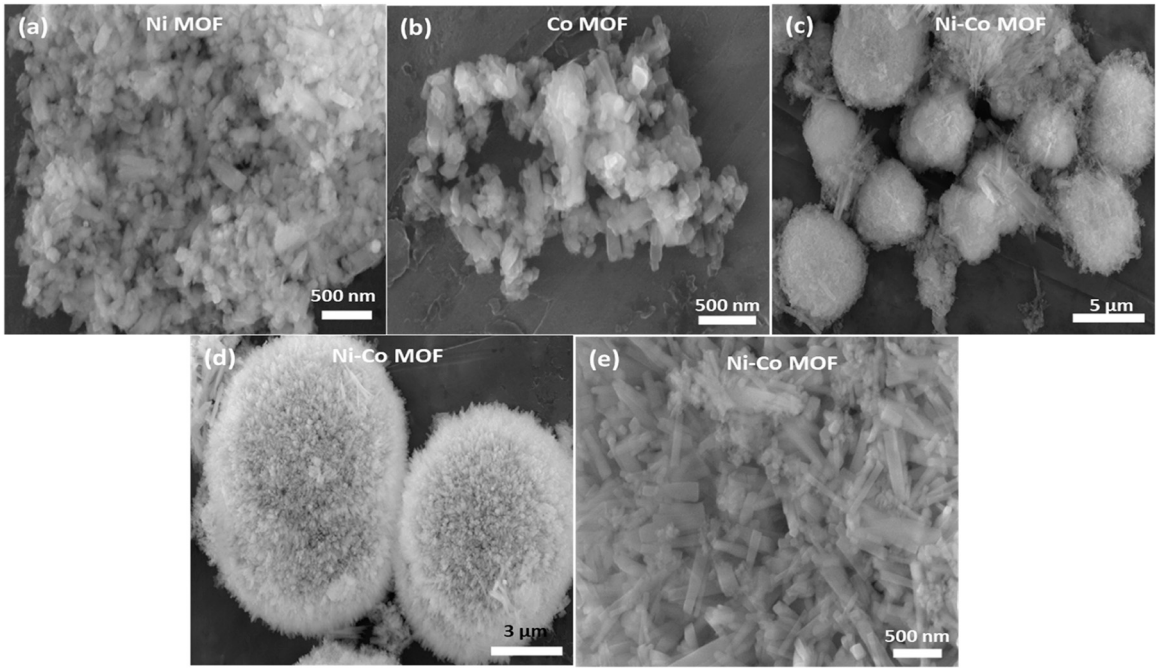

Fig. 3 HRSEM images of (a) Ni MOF, (b) Co MOF and (c–e) Ni–Co MOF.

matches Ni–Co MOF precisely. In addition, the SEM colour mapping is also shown in Fig. S2.

To understand the surface phenomena of Ni–Co MOF, XPS characterisation has been performed as shown in Fig. 4. The C 1s spectra deconvoluted into three peaks with the peak positions of 284.74, 285.76 and 288.4 eV assigned respectively to C–C, C–O/C–N and O–C═O/C═O bonds.[17,25,26] The highest binding energy peak among these is attributed to the carboxyl group (O–C═O) in aromatic rings, which is from the organic ligand BTC[28,29] as shown in Fig. 4b. Fig. 4c shows

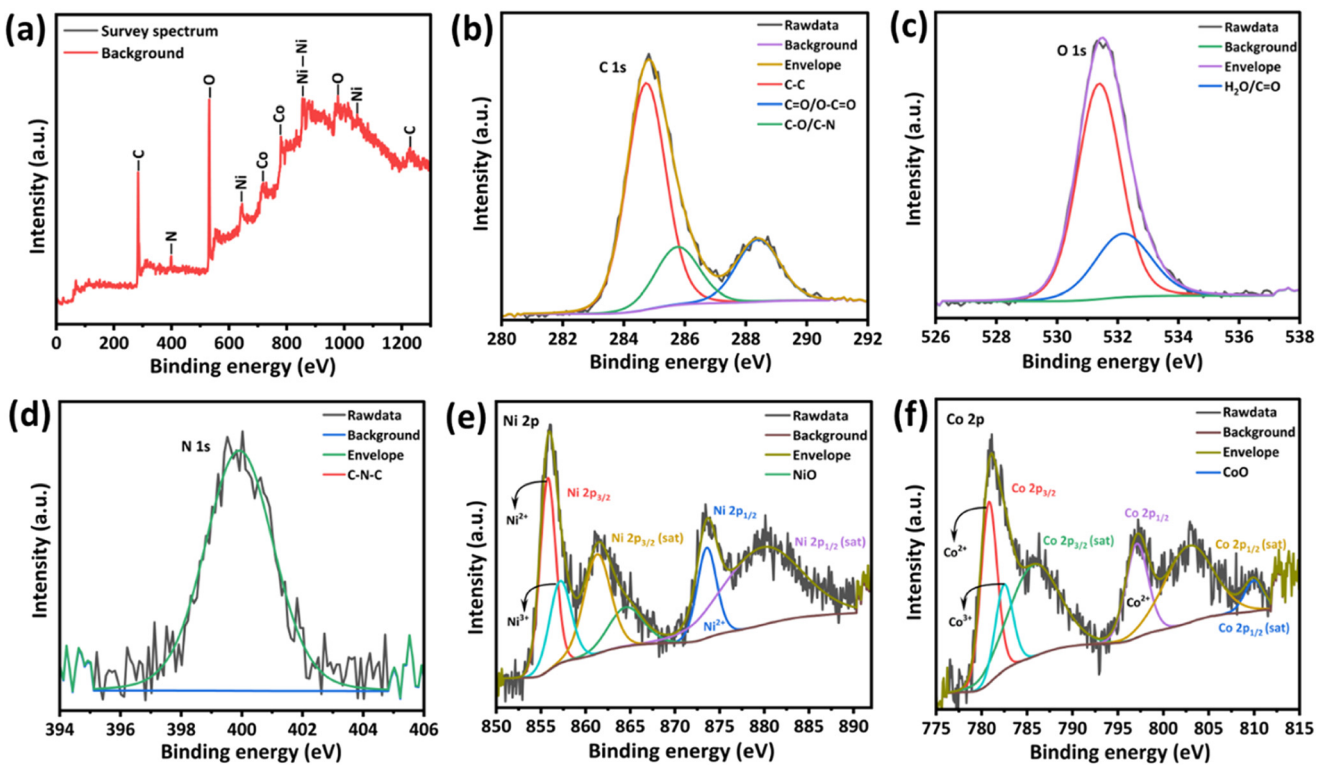

Fig. 4 XPS of (a) survey scan, (b) C 1s, (c) O 1s, (d) N 1s, (e) Ni 2p, and (f) Co 2p.

Open Access Article. Published on 20 February 2026. Downloaded on 5/25/2026 6:49:37 PM. This article is licensed under a Creative Commons Attribution-NonCommercial 3.0 Unported Licence.

that the O 1s spectra of Ni–Co MOF exhibited peaks at the positions of 531.39 eV and 532.18 eV, respectively. The peak with lower binding energy signifies the defect sites with the least oxygen atom coordination and also provides information on adsorbed oxygen species on the surface. The peak of 532.18 eV corresponds to physiosorbed/chemisorbed water molecules,[27,28] and the literature also suggests that it could contribute to the C=O bond.[17] The peak at 399.9 eV on the N 1s spectra of Ni–Co MOF corresponds to the C–N–C group from the DMF solvent[29] as seen in Fig. 4d.

Fig. 4e shows the spectra of Ni 2p; the peaks observed at 855.76 eV and 873.56 eV correspond to the spin-orbit characteristics of Ni^{2+} ascribed to Ni $2p_{3/2}$ and Ni $2p_{1/2}$, respectively. Their satellite peaks were found correspondingly at 861.28 eV and 879.75 eV. The spin energy separation was found to be 17.8 eV from the primary peaks of Ni $2p_{3/2}$ and Ni $2p_{1/2}$.[25] The peak observed at 857.19 eV corresponds to the Ni^{+} oxidation state, ascribed to Ni $2p_{3/2}$ and its respective satellite peak was found at 864.52 eV, thus corresponding to the presence of NiO.[30] The possible reason for the Ni^{3+} presence could be due to the vacancy created in the Ni lattice: to neutralise the charge of the crystal, Ni^{2+} ions were oxidised to Ni^{3+}. Fig. 4f shows the Co 2p spectra; the peaks observed at 780.80 eV and 797.08 eV correspond to the spin–orbit doublet of Co^{2+} ascribed to Co $2p_{3/2}$ and Co $2p_{1/2}$, respectively. Their respective satellite peaks are situated at 785.74 eV and 802.78 eV.[9,31] In addition, the spin energy separation was found to be 16.28 eV. The peak that arose at 782.5 eV indicates the presence of the Co^{3+} oxidation state, suggesting the presence of the lattice plane (111), which provides higher catalytic activity.[32,33] Also, an appearance of a less intensive peak at 810 eV is possibly due to the phenomena of photoionisation due to the presence of Co oxides.[33]

To determine the surface area and pore size of the synthesised Ni–Co MOF material, the BET characterisation has been performed. Fig. 5a illustrates the type IV(a) adsorption isotherm, which indicates the material is likely to be mesoporous in nature. The type IV(a) isotherm is associated with capillary condensation phenomena, which exhibits hysteresis. This phenomenon occurs when there is a varying pore size distribution in the material.[34] To determine the number of surface-active sites in the material, the BET monolayer capacity was estimated as 5.192 $cm^3\ g^{-1}$ from the BET plot shown in Fig. 5b. Through that, the resultant surface area was estimated as 22.616 $m^2\ g^{-1}$, which corresponds to the total number of active sites on the material surface. Additionally, the BJH (Barrett–Joyner–Halenda) plot has been used to view the pore size distribution of the material. From Fig. 5c, it is evident that the pore size distribution has varied, ranging from mesoporous to macroporous. As a result of this variance, we observed a type IV(a) isotherm with hysteresis.

3.2. Evaluation of sensor properties

The behaviour of the AA analyte on the working electrode was examined through *I–t* tests under open circuit potential/zero gate voltage conditions. The gate-source voltage (V_{GS}) of the system was set to zero voltage and the experiments were carried out by monitoring the change in the drain current ΔI_D upon the successive addition of increasing concentrations of ascorbic acid. Catalyst distribution plays a critical role in the electrochemical performance of an electrode. The surface morphology of the Ni–Co MOF/CP has been characterised through SEM and digital microscopy, as shown in Fig. S3. It was observed that the uneven distribution and particle aggregation of the Ni–Co MOF over the surface of the carbon paper offered a heterogeneous electrode surface, which most probably is due to the coffee ring effect upon solvent evaporation.

Most types of particle-modified electrodes (PMEs) operate based on a principle known as adsorptive preconcentration, wherein the target analyte is adsorbed and accumulated by the catalyst prior to electrochemical detection. For PMEs, a sufficiently/optimally thick layer of the catalyst is preferred due to its ability to enhance sensitivity. An optimised thick layer of the catalyst results in a higher analyte adsorption, which in turn leads to increased signal intensity. In this scenario, it is crucial to ensure a strong adsorption of the analyte, along with a swift desorption process, *i.e.* the catalyst must efficiently adsorb the analyte and release it effectively.

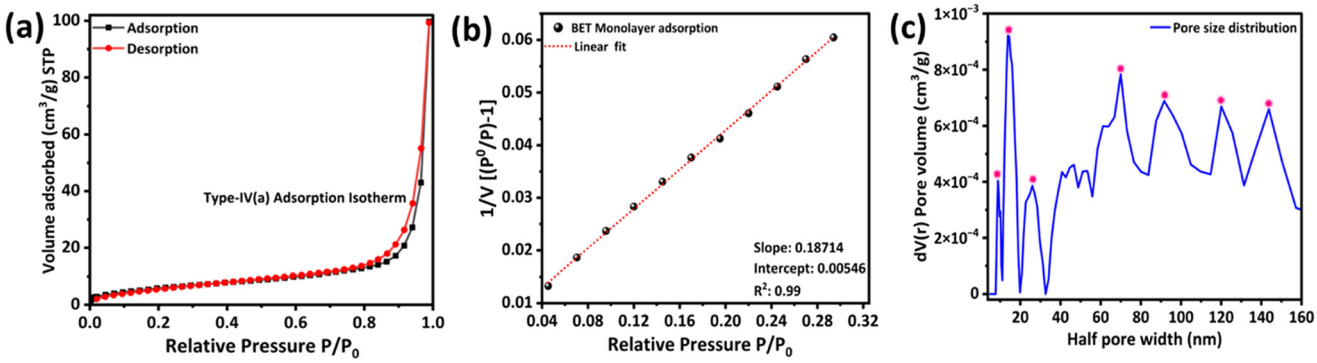

Fig. 5 BET (Brunauer–Emmett–Teller) characterisation of Ni–Co MOF: (a) isotherm plot, (b) linear plot and (c) BJH (Barrett–Joyner–Halenda) plot.

© 2026 The Author(s). Published by the Royal Society of Chemistry

Open Access Article. Published on 20 February 2026. Downloaded on 5/25/2026 6:49:37 PM. This article is licensed under a Creative Commons Attribution-NonCommercial 3.0 Unported Licence.

However, if the adsorption is too strong, the analyte may not desorb properly, hindering the electrode's ability to carry out electrochemical detection. On the other hand, if the analyte is released too quickly, it may not accumulate sufficiently on the electrode surface, leading to reduced sensitivity. Hence it is essential to balance these two factors to enhance PME performance effectively. This ensures that the analyte is readily available for electrochemical detection, allowing the released analyte to spread through the electrolyte solution and diffuse through the electrode, facilitating the occurrence of the redox reaction.[35]

Herein, the experiment to examine how the catalyst loading effect deposited on the CP WE through the drop-casting method influences electrode performance in terms of target sensing, electrode kinetics, sensitivity, and limit of detection has been performed.

To comprehend the binding affinity of the analyte onto the prepared electrode, the calibration curve was fitted by using the Hill–Langmuir isotherm model, which describes that the adsorption of the analyte to the catalyst is a cooperative phenomenon, *i.e.*, the analyte at one site of the catalyst will influence the other binding site of the same catalyst.[36,37]

$$q_e = \frac{qs_H \times C_e^n H}{K_D + C_e^n H} \quad (1)$$

where, q_e – amount of adsorbate in the adsorbent at equilibrium (mg g^{-1}); qs_H – Hill isotherm maximum uptake saturation (mg L^{-1}), *i.e.* the adsorbent surface is fully covered with adsorbate molecules, and no more adsorption can occur; n – Hill coefficient, which describe the degree of cooperativity ($n > 1$ indicates positive cooperative binding, which means that the binding of first analyte molecule at one active site of a catalyst enhances the binding affinity of others; $n < 1$ indicates negative cooperative binding, which means that the binding of first analyte molecule at one active site of a catalyst decreases the binding affinity of a second molecule; $n = 1$ indicates non-cooperative binding, which means that the binding of one analyte molecule does not affect the binding of others); K_D – complex dissociation constant.

The above model described by eqn (1) was modified to our focus of subject as follows:[38]

$$\Delta I_D = \frac{I_{max} \times C_{AA}^n}{K_d + C_{AA}^n} \quad (2)$$

where, I_{max} – saturation response; C_{AA}– concentration of ascorbic acid.

Hill–Langmuir plots of different catalyst loadings indicate that the surface adsorption of the electrode is showing multisite adsorption with positive cooperativity. There is always a prevalent notion that the lower K_d value facilitates higher binding affinity and leads to detecting the lower LOD.[39]

Fig. 6a shows the effect of weight loading the AA detection of 320 μg Ni–Co MOF catalyst loading has demonstrated a

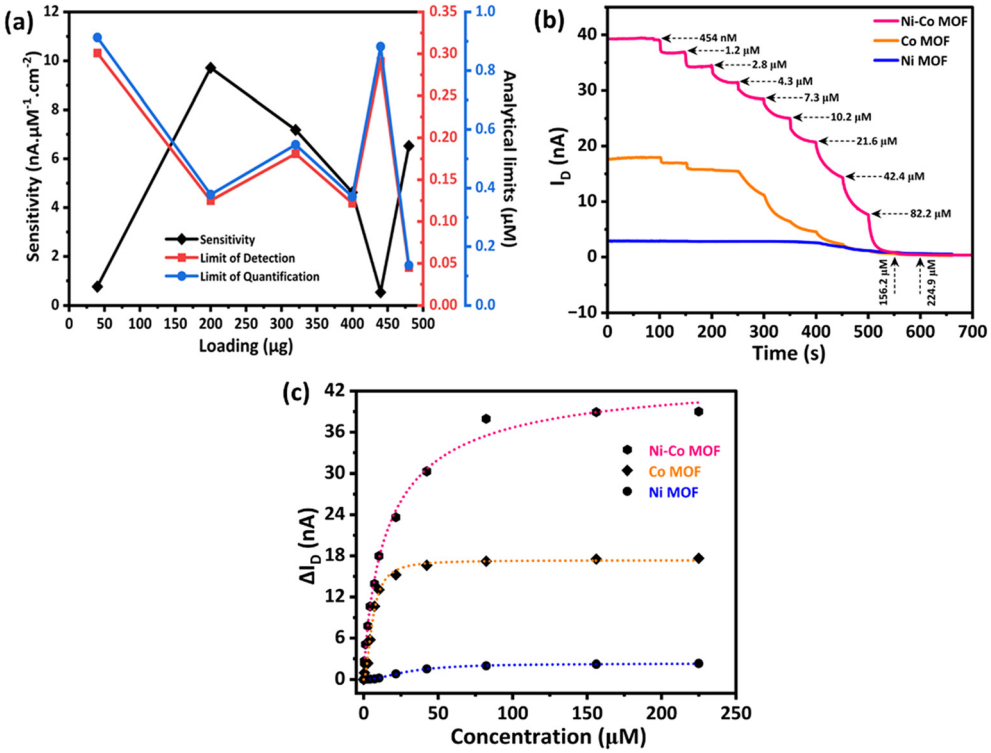

Fig. 6 a) Sensitivity, LOD and LOQ characteristics of tested Ni-Co MOF/CP electrodes at different weight loading amounts on carbon paper towards AA, b) dynamic calibration curves and c) calibration plot of 480 μg loaded Ni-MOF/CP following the Hill–Langmuir isotherm.

© 2026 The Author(s). Published by the Royal Society of Chemistry

Open Access Article. Published on 20 February 2026. Downloaded on 5/25/2026 6:49:37 PM.
This article is licensed under a Creative Commons Attribution-NonCommercial 3.0 Unported Licence.

pattern that is comparable to the trend observed in the 200 μg Ni–Co MOF-coated electrode. Among all the tested Ni–Co MOF catalyst loadings, 440 μg loading has shown the lowest sensitivity and weak signal intensity to identify the variation occurred for each added concentration. It might be owing to the fact of rapid desorption of the analyte from the adsorptive layer due to inadequate time for catalyst accumulation on the electrode surface.

While increasing the amount of Ni–Co MOF catalyst loaded on the CP electrode to 480 μg, a significant variation in drain current (I_D) for all the added AA concentrations has been registered. The best results in terms of good sensitivity and lower limit of detection were obtained for the 480 μg Ni–Co MOF coated electrode. However, the Hill coefficient value of 480 μg –Ni–Co MOF coated electrode has shown negative cooperativity behaviour, which states that the binding of AA at one site of the Ni–Co MOF catalyst decreases the rate of subsequent binding or the likelihood of forming a next layer is reduced because each additional AA molecule that binds with lower affinity potentially reduces the multisite adsorption. Based on classic theory, only positive cooperative interactions would provide enhanced sensitivity with high electrochemical performance. However, as it was demonstrated by Ha *et al.*,[40] the negative cooperative interaction can also produce ultrasensitive and threshold responses[47] when the analyte depletion effect is involved. This finding suggests that when the catalyst's accumulation of analyte is insufficient or not fully saturated, it functions as a buffer, momentarily binding analyte molecules without inducing a significant reaction. As the analyte concentration increases, the buffering effect persists until a critical threshold is attained, and then the reaction abruptly accelerates, resulting in increased catalytic activity and greater sensitivity.

Fig. 6a shows the different weight loads on the Ni–Co-MOF on CP towards AA spiked at a regular interval of 100 s. The results suggest that increasing the weight increases the sensitivity and reduces the LOD and LOQ from 40 to 200 μg. However, further increasing reduced the sensitivity at 320 μg. And these trends follow the consecutive 400 and 440 μg of catalysis on CP. But at 480 μg, the sensitivity increases again. It is noteworthy that, though the sensitivity is a bit compromised compared to 200 μg, the LOD and LOQ have reduced approximately 2.5 times. The estimated LOD for 480 μg Ni–Co MOF-coated electrode was 45.1 nM and a limit of quantification (LOQ) of 136 nM, which lies in the range of AA concentration in human body fluids.

Through the comparison of the results on the performance of monometallic MOF/CP materials with the Ni–Co MOF/CP, it is observed that although the occupation of Co atoms in the Ni–Co MOF composition is lower than that of Ni atoms, yet it has facilitated effective catalytic activity for the oxidation of AA process[41] and enables the quantification. According to the recently reported literature, the synergistic incorporation of Ni and Co in NiCo MOF significantly enhances electrical conductivity, reaching an average value of 0.058 mS cm^{-1}—34 times higher than that of monometallic Ni MOF (0.0017 mS cm^{-1}).[42] Also, density functional theory (DFT) calculations reveal that the addition of Co^{2+} introduces additional electron transport pathways and markedly increases carrier concentration, resulting in 19 more electrons at the Fermi level compared to Ni MOF. This improved conductivity translates to superior electrochemical performance overall. Consistent with these observations, our study demonstrates that NiCo MOF enables highly sensitive ascorbic acid detection down to nanomolar concentrations, highlighting the practical benefits of this bimetallic synergy in proton-coupled sensing applications. Also, the addition of Co MOF in the bimetallic preparation permits overcoming the instability of Ni MOF, and their synergistic role paves the way for high-sensitivity AA detection at nanomolar concentrations.

The study mainly relies on open circuit potential (OCP), which is an inherent potential that arises between the working electrode and the electrolyte solution as shown in Fig. 6b, and it is quantified using a reference electrode. The graph shows that Ni–Co MOF exhibits higher response towards AA compared to Ni MOF and Co MOF. This phenomenon is alternatively referred to as electrochemical cell potential, equilibrium potential, or corrosion potential (E_0). It bestows the information of the electrode's reactivity and surface reaction rate with respect to the electrolytic medium. Major advantages of OCP are minimal power consumption, less interference by contaminants, and simplifying and miniaturising electrochemical systems.[43]

We monitored the *I–t* response after the current had fully stabilized at open circuit potential (OCP). Capacitive currents from interfacial electric double-layer (EDL) charging follow the standard equation (3):

$$I_c = C_{dl} \cdot \frac{dE}{dT} \quad (3)$$

where, I_c is the non-faradaic charging current, C_{dl} is double-layer capacitance and $\frac{dE}{dT}$ is the rate of potential change.[44]

The *I–t* trace in Fig. 6b shows rapid stabilization to a constant current before analyte addition, confirming equilibrium OCP ($dE/dt = 0$). From the equation, when $dE/dt = 0$, $I_c = 0$. Therefore, persistent capacitive contributions from EDL charging were ruled out.

Regarding electronic conduction (sustained net faradaic current), OCP measurements inherently involve a high-impedance voltmeter/electrometer (input resistance typically $>10^{12}$ Ω), which ensures negligible current through the external circuit and prevents polarization or disturbance of the equilibrium (zero-net-current condition). At OCP, anodic and cathodic processes balance precisely ($I_{net} = 0$ as per mixed potential theory), providing no driving force for ongoing redox or bulk electronic conduction.[44] The low stabilized background current (~nA range) reflects no significant electronic pathways. Additionally, the *I–t* curve

© 2026 The Author(s). Published by the Royal Society of Chemistry

Open Access Article. Published on 20 February 2026. Downloaded on 5/25/2026 6:49:37 PM. This article is licensed under a Creative Commons Attribution-NonCommercial 3.0 Unported Licence.

included for the bare carbon paste (CP) electrode (Fig. S7, SI) provides further confirmation: no electrochemical response is observed even after the introduction of ascorbic acid. This is in agreement with the established property of pure carbon as a purely electronic conductor, incapable of proton conduction.

Therefore, considering the fact that ascorbic acid can oxidise at such low potentials[45] the following ionisation equilibria will be established in solution at close to neutral pH (pKa1 = 4.17, pKa2 = 11.6), resulting in proton release and ascorbate anion formation as shown in eqn (4).[46]

$$\text{Ascorbic Acid } (C_6H_8O_6) \rightleftharpoons \text{Ascorbate } (C_6H_7O_6^-) + H^+ \quad (4)$$

In general, aromatic carboxylate-based MOFs have demonstrated proton conduction behaviour.[47] According to reports, Ni and Co-based MOFs are good proton (H^+) conductors, and using Nafion as a binder may further boost H^+ conduction as it is an ideal proton conductor.[47–49] Fig. 6c shows the calibration plot of the sensors towards AA; it shows a higher response due to proton conduction in the prepared electrode (Ni–Co MOF/CP with Nafion as a binder), which is possibly caused by the presence of sulfonate groups ($-SO_3^-$), carboxyl (–COOH) groups, and Ni^{2+}/Co^{2+} metal nodes. In the instance of Nafion in proton conduction, the Grotthus mechanism takes precedence over the vehicular mechanism because its concentration is 1% and the environment is primarily made of weakly bound water/high water content.[50] Similarly, in 1,3,5-benzene tricarboxylic acid (BTC), the carboxyl group may serve either as a proton donor (–COOH) or acceptor (–COO–), and the water molecule links these two, creating proton hopping pathways.[51]

Furthermore, the higher composition of Ni in Ni–Co MOF with BTC as a linker has been demonstrated to improve the electrochemical reaction, most likely owing to increased charge transport, which supports the presented results.[52,53] The electrodes are initially stabilised in a PBS environment before carrying out AA sensing, implying that the change in the drain current after the addition of AA is not through the interaction of ions present in the PBS. After the addition of AA, the difference in the drain current was observed as it undergoes reaction given by eqn (4). As the concentration of AA increases, the drain current decreases relatively with increasing H^+ concentration and conduction.

The main cause for the EGFET drain current change ΔI_D is the conduction of H^+ *via* Ni–Co MOF and Nafion. The detection of AA is driven by proton conduction through both Grotthuss and vehicular mechanisms, with the former being the predominant mechanism, considering the composition of the electrode (Ni–Co MOF with Nafion as binder), the aqueous medium, and the released H^+ during the oxidation of ascorbic acid. Table 1 reports the comparison of performance metrics from recently reported MOF-based sensors and OCP-based approaches and the properties of the sensor developed in the present work for AA assessment.

3.3. SKP study

The study of the sensing mechanism using a surface Kelvin probe (SKP), which measures constant potential difference (CPD) changes upon the addition of AA, has provided valuable insights into the sensor's performance. Fig. 7(a) shows the 3D raster scan of the electrodes and they exhibit positive CPD for Ni MOF/CP, Co MOF/CP, and Ni–Co MOF/CP coated electrodes, which may be due to similar p-type semiconductor behaviour.[59,60] The three MOF materials showed higher work function values in comparison to bare CP, indicating that the presence of sensing materials is able to increase proton-conducting nature. The work function of the reference gold (Au) tip is 5.1 eV. The Ni MOF/CP sensor has shown a higher work function value of 5.62 eV compared to other electrodes coated with Co MOF (5.53 eV), Ni MOF (5.36 eV), and CP (5.17 eV), respectively.[59,60]

Fig. 7b shows a 3D raster scan with varying concentrations of ascorbic acid added for the Ni–Co MOF sensing electrode. The work function of an electrode with 1.2 μM of ascorbic acid showed a 0.08 eV difference after cycling. However, as the concentration increased from 1.2 μM to 156.2 μM, the work function decreased from 5.18 to 5.08 eV due to charge transfer from the ascorbic acid to the sensing electrode. This decrease in work function results confirms the proposed sensing mechanism of AA. Whereas, the work function difference between 42.4 μM and 156.2 μM showed a 0.01 eV difference, possibly due to a sudden

Table 1 The composition and performance metrics of previously developed MOF-based sensors and OCP-based approaches

N	Material	Method	Applied voltage	Linear range	Analyte, LOD	Ref
1	Carbon electrodes coated with TiO_2–Cu-MOF composites	EGFET	0.6 V	15 nM to 14.38 mM	AA, 12 nM	54
2	Mn-OM-MOF /CP[a]	EGFET		5 to 240 μM	AA, 0.26 μM	55
3	I_2@FeTHQ[b]	EC	−0.2 V	1–1200 μM	AA, 20 nM	56
4	Eu MOF	Fluorescence	NA	0–3.0 mM	AA & ascorbate oxidase, 0.32 μM	57
5	$Cu_3(HHTP)_2$/SPE	EC (DPV)	0.2 V	25–1645 μmol L^{-1}	AA, 2.4 μmol L^{-1}	58
6	KSC/GOD[c]	EC	0	0.03–10.0 mM	Glucose, 10 μM	16
7	NiCo-MOF/CP	EGFET	0	454 nM to 224.9 μM	45.1 nM	This work

[a] Mn MOF as an enzyme mimic by incorporating $H_2PcP_8OH_{16}$ coated on carbon paper. [b] Iodine doped Conductive metal–organic frameworks. [c] Kenaf stem (KSC) was used to construct a KSC microelectrode (denoted as KSCME) which was subsequently used to load glucose oxidase.

Open Access Article. Published on 20 February 2026. Downloaded on 5/25/2026 6:49:37 PM.
This article is licensed under a Creative Commons Attribution-NonCommercial 3.0 Unported Licence.

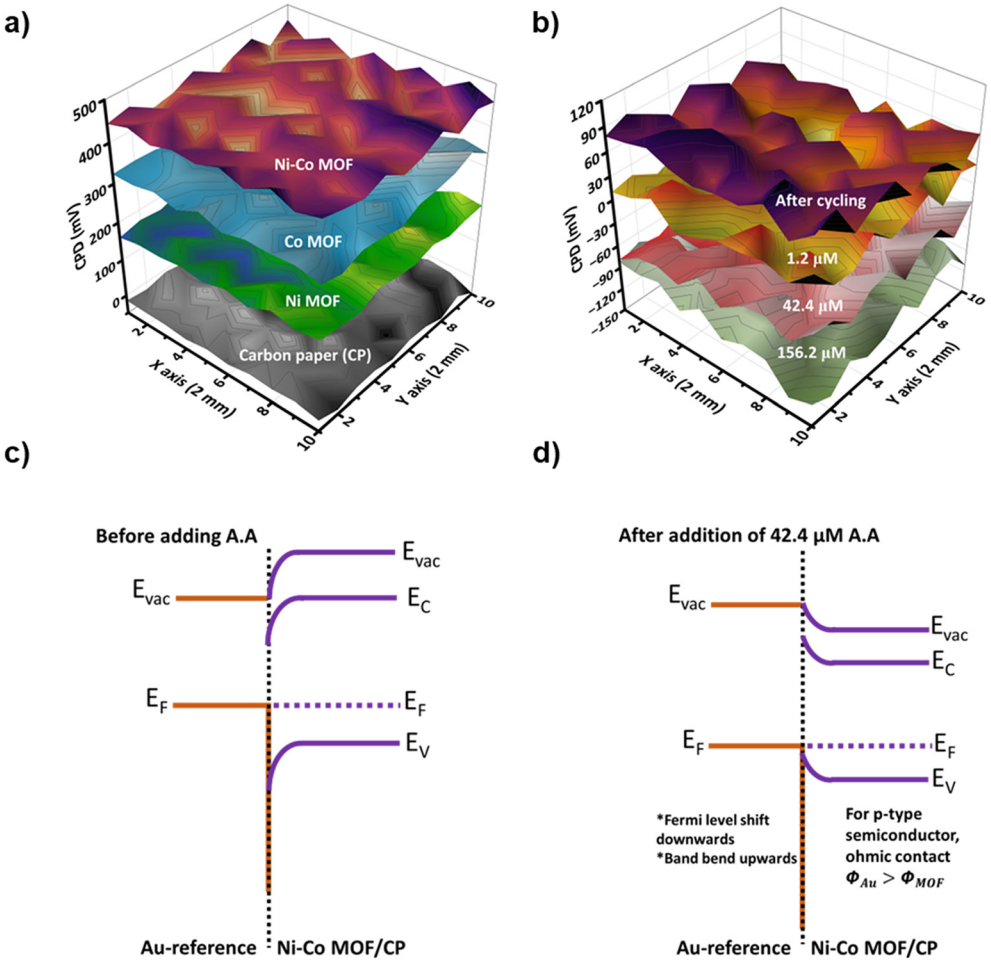

Fig. 7 SKP measurements representing: 3D raster scans of (a) CP with Ni-MOF, Co-MOF and Ni–Co MOF and (b) Ni–Co MOF/CP after addition of AA; band bending diagrams between the electrode and Au tip c) before and d) after addition of AA.

pH decrease due to the release of H^+ and adsorption of ascorbate ion during the AA oxidation. With the increasing concentration of ascorbic acid, no significant pH shift was registered; thereby the change in the drain current is dominated mainly by proton conduction, which explains the reduced difference in work function between the concentrations of 42.4 µM, and 156.2 µM.

The changes in work function occurring for the Ni–Co MOF catalyst-coated CP electrode can be used to explain the band bending phenomena. During the external contact, the charge is transferred from the material with a lower work function to one with a higher work function. It causes the space charge region (SCR) to develop and an inherent electric field to be established. Fig. 7c illustrates the charge diffusing from metal–Au (reference) to the Ni–Co MOF until equilibrium is reached, where the Fermi levels align. During equilibrium, a depletion layer forms, generating an internal field that aids in band bending.[61] The energy level diagram without ascorbic acid shows upward band bending and work function values of 5.17 eV and 5.62 eV for CP and Ni–Co MOF/CP, respectively.

The work function values of Ni-MOF/CP decrease after continuous cycling at 5.26 eV due to the cancellation of the surface depletion barrier, resulting in upward band bending. Upon the addition of ascorbic acid, the Fermi level of $E_{F(MOF)}$ shifts upwards, and the band bends downwards to align with the Fermi level of $E_{F(Au)}$. The oxidation of ascorbic acid results in a decrease in the work function with a 42.4 µM concentration of ascorbic acid added to a Ni–Co MOF/CP electrode Fig. 7d. This decrease from 5.17 eV to 5.08 eV indicates that charge transfer is occurring from ascorbic acid (adsorbate) to the sensing electrode. On the other hand, when the work function of the material decreases upon binding with any adsorbate, it implies that the charge transfer is taking place from the adsorbate to the electrode.[62] Here, after AA binds with the electrode, the ascorbate ion and H^+ released interact with the electrode, facilitating a change in the work function of the Ni–Co MOF/CP.[63]

Fig. 8a represents the interference study of the fabricated Ni–Co MOF/CP electrode. The selectivity tests were run through consecutive addition of ascorbic acid (3.5 µM), glucose (5 mM), fructose (100 µM), sucrose (500 µM), lactose (100 µM) and nicotine (100 µM) on PBS 1× background

© 2026 The Author(s). Published by the Royal Society of Chemistry

Open Access Article. Published on 20 February 2026. Downloaded on 5/25/2026 6:49:37 PM.
This article is licensed under a Creative Commons Attribution-NonCommercial 3.0 Unported Licence.

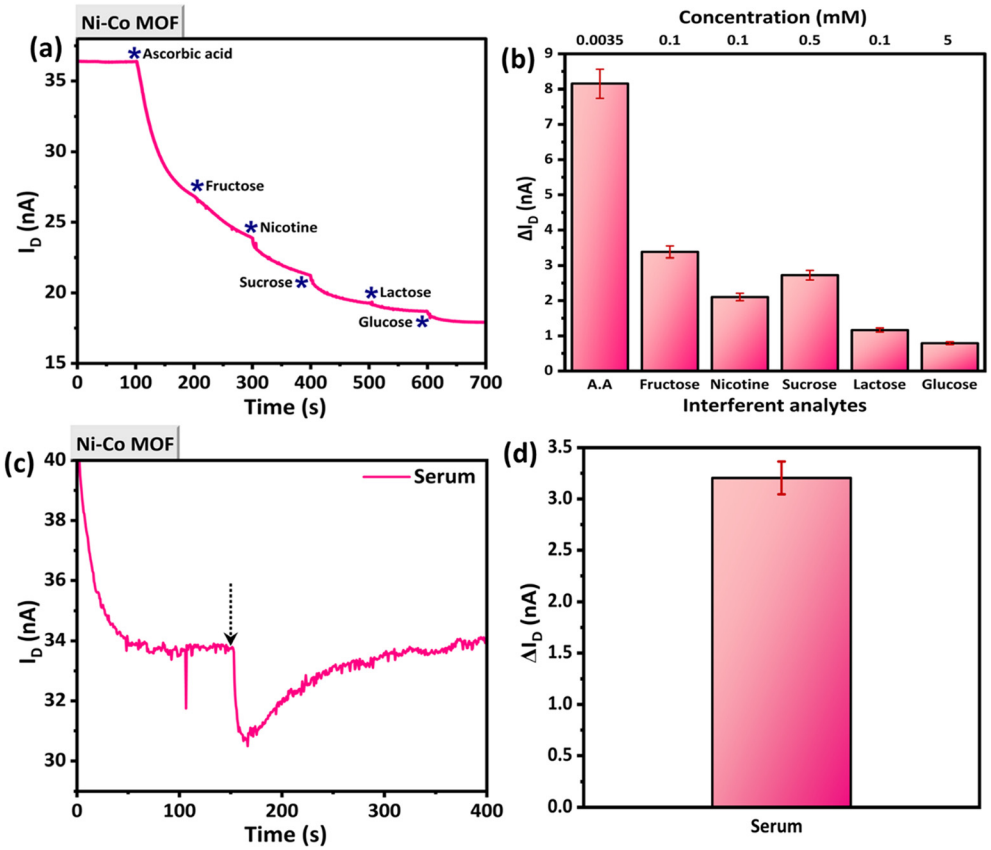

Fig. 8 (a) *I–t* curve of Ni–Co MOF/CP selectivity test against common interfering molecules, (b) bar chart representation of selectivity test with error bar, (c) *I–t* curve of Ni–Co MOF/CP electrode for AA assessment in real blood serum sample, (d) bar chart representation of current response of real blood serum sample where error bars represent the uncertainity of fitting (95% confidence interval).

solution upon *I–t* characteristic response registration. The enhanced selectivity of the developed Ni–Co MOF/CP electrode for ascorbic acid was registered; the change in the drain current (ΔI_D) for AA was significantly higher with respect to all the tested interferent molecules. The negligible interference on the Ni–Co MOF electrode response variation gave lactose and fructose addition, while some minimal interference was noticed for glucose, nicotine and sucrose. Fig. 8b shows the graph of the sensors' response towards AA and its interactions. It is interesting to see that AA is at least 20-fold less concentrated compared to nicotine and all carbohydrates.

To verify the reliability of our experiment, we have performed an analysis of blood serum using the Ni–Co MOF/CP electrode in EGFET configuration as shown in Fig. 8c. The typical concentration of AA found in blood serum ranges from approximately 11 to 80 μM. In this experiment, we have spiked 500 μl of serum into 5 ml of PBS. Taking into consideration the dilution factor of 10, the concentration of AA was found to be 10.85 μM, which was in good correlation with the 10.447 μM value found with the standard HPLC method for the same blood serum sample. It was determined that the recovery ratio was 103.85%. Hereby, the EGFET-based biosensor can be recommended for real-time analysis of AA in biological liquids.

4. Conclusion

A novel Ni–Co MOF catalytic coating has been synthesised for the detection of ascorbic acid (AA), focusing on its application in scurvy diagnosis. The EGFET sensor modified with the Ni–Co MOF catalyst and operating undert open circuit potential (OCP) conditions assessed AA through a mechanism primarily driven by proton conduction. Through surface Kelvin probe analysis, it was demonstrated that the sensing mechanism involves both proton conduction and ascorbate ion interaction, with proton conduction being dominant. The developed bimetallic Ni–Co MOF/CP electrode outperformed the single metal-based Ni MOF and Co MOF, demonstrating a wide AA detection range from 454 nM to 224.9 μM, with a response time of less than 7 seconds, LOD of 45.1 nM, and LOQ of 136 nM. The interference studies have demonstrated an enhanced selective response of the developed Ni–Co MOF/CP electrode to AA against common interfering molecules present in biological samples at their physiological levels. The good correlation between AA concentration assessed by the developed Ni–Co MOF/CP sensor in real blood samples and the AA amount found with the standard HPLC method and a recovery of 103.85% have been obtained, highlighting its reliability for real-time analysis of AA in biological liquids. Overall, the OCP-based

Open Access Article. Published on 20 February 2026. Downloaded on 5/25/2026 6:49:37 PM. This article is licensed under a Creative Commons Attribution-NonCommercial 3.0 Unported Licence.

extended-gate field-effect transistor (EGFET) has shown a promising approach for miniaturised and low-power sensor development.

Author contributions

A. V.: writing – review and editing, and investigation; G. P. K.: writing – review and editing, and investigation; K. P.: writing – review and editing; S. M.: writing – review and editing; L. L: writing – review and editing, and supervision; S. V. J.: writing – review and editing, and supervision; C. D. N.: writing – review and editing, and supervision; Y. S.: conceptualization, supervision, writing – review and editing. All authors have read and agreed to the published version of the manuscript.

Conflicts of interest

There are no conflicts to declare.

Data availability

The data supporting this article have been included as part of the supplementary information (SI).

Supplementary information: SI file contain EDX, SEM, SEM-EDS color mapping of Ni–Co MOF/CP; transfer characteristics of electrodes, calibration plot and *I–t* curve of pure CP. See DOI: https://doi.org/10.1039/d5sd00217f.

Acknowledgements

This work was supported by the Science and Engineering Research Board (SERB), Department of Science and Technology (DST), Government of India, under ECRA (file no.: ECR/2017/001218) and CRG (file no.: CRG/2021/006647). We acknowledge SRMIST for providing the necessary characterization facilities.

References

1 S. Rowe and A. C. Carr, *Nutrients*, 2020, **12**, 2008.
2 A. C. Carr and S. Rowe, *Nutrients*, 2020, **12**, 1963.
3 R.-L. Lu, J.-W. Guo, B. Sun, Y.-L. Chen and D.-Z. Liu, *Front. Nutr.*, 2023, **10**, 1265334.
4 S. Thiemann, V. Cimorelli and N. M. Bajwa, *Front. Endocrinol.*, 2022, **13**, 968015.
5 J. A. Olson and R. E. Hodges, *Am. J. Clin. Nutr.*, 1987, **45**, 693–703.
6 J. P. Sebastian and L. Mark, *Oral Dis.*, 2016, **22**, 463–493.
7 S. Skrovankova, J. Mlcek, J. Sochor, M. Baron, J. Kynicky and T. Jurikova, *Int. J. Electrochem. Sci.*, 2015, **10**, 2421–2431.
8 J. van der spiegel, I. Lauks, P. Chan and D. Babic, *Sens. Actuators*, 1983, **4**, 291–298.
9 S. Gao, Y. Sui, F. Wei, J. Qi, Q. Meng, Y. Ren and Y. He, *J. Colloid Interface Sci.*, 2018, **531**, 83–90.
10 X. Zhao, J. Feng, J. Liu, J. Lu, W. Shi, G. Yang, G. Wang, P. Feng and P. Cheng, *Adv. Sci.*, 2018, **5**, 1700590.
11 D. Li, A. Yadav, H. Zhou, K. Roy, P. Thanasekaran and C. Lee, *Glob. Chall.*, 2024, **8**, 2300244.
12 M. Baghayeri, M. Ghanei-Motlagh, R. Tayebee, M. Fayazi and F. Narenji, *Anal. Chim. Acta*, 2020, **1099**, 60–67.
13 M. Lu, Y. Deng, Y. Luo, J. Lv, T. Li, J. Xu, S.-W. Chen and J. Wang, *Anal. Chem.*, 2018, **91**, 888–895.
14 C. Kokkinos, A. Economou, A. Pournara, M. Manos, I. Spanopoulos, M. Kanatzidis, T. Tziotzi, V. Petkov, A. Margariti and P. Oikonomopoulos, *Sens. Actuators, B*, 2020, **321**, 128508.
15 S. Lee, N. Kwon, Y. Yoon, J. Yoon, J. G. Jang, W. Lee, J.-H. Lee, C. Park and T. Lee, *Nanoscale*, 2025, **17**, 22235–22247.
16 Y. Song, D. Su, Y. Shen, H. Liu and L. Wang, *Anal. Bioanal. Chem.*, 2017, **409**, 161–168.
17 Q. Wang, Y. Wang, Z. Zhang, Y. Tong and L. Zhang, *Microchim. Acta*, 2017, **184**, 4107–4115.
18 S. Zhao, L. Zeng, G. Cheng, L. Yu and H. Zeng, *Chin. Chem. Lett.*, 2019, **30**, 605–609.
19 L. Peng, S. Wu, X. Yang, J. Hu, X. Fu, M. Li, L. Bai, Q. Huo and J. Guan, *New J. Chem.*, 2017, **41**, 2891–2894.
20 D. Lin, Y. Zheng, X. Feng, Y. You, E. Wu, Y. Luo, Q. Qian and Q. Chen, *J. Mater. Sci.*, 2020, **55**, 5190–5202.
21 E. Irandoost, N. S. Barekati, H. Farsi, A. Farrokhi, G. Horvath and Z. Li, *Appl. Energy Combust. Sci.*, 2024, **17**, 100240.
22 M. G. Radhika, B. Gopalakrishna, K. Chaitra, L. K. G. Bhatta, K. Venkatesh, M. K. S. Kamath and N. Kathyayini, *Mater. Res. Express*, 2020, **7**, 54003.
23 F. Israr, D. Chun, Y. Kim and D. K. Kim, *Ultrason. Sonochem.*, 2016, **31**, 93–101.
24 D. L. Pavia, G. M. Lampman, G. S. Kriz and J. R. Vyvyan, *Introduction to Spectroscopy*, Brooks/Cole, Cengage Learning, 2009.
25 J. Xu, C. Yang, Y. Xue, C. Wang, J. Cao and Z. Chen, *Electrochim. Acta*, 2016, **211**, 595–602.
26 R. Palani, V. Anitha, C. Karuppiah, S. Rajalakshmi, Y.-J. J. Li, T.-F. Hung and C.-C. Yang, *ACS Omega*, 2021, **6**, 16029–16042.
27 C. Belkessam, S. Bencherif, M. Mechouet, N. Idiri and J. Ghilane, *Chem*, 2020, **85**, 1710–1718.
28 M. Cheng, H. Fan, Y. Song, Y. Cui and R. Wang, *Dalton Trans.*, 2017, **46**, 9201–9209.
29 H. Wang, H. Zou, Y. Liu, Z. Liu, W. Sun, K. A. Lin, T. Li and S. Luo, *Sci. Rep.*, 2021, **11**, 21414.
30 P. Thangasamy, S. Shanmuganathan and V. Subramanian, *Nanoscale Adv.*, 2020, **2**, 2073–2079.
31 N. Yang, H. Song, X. Wan, X. Fan, Y. Su and Y. Lv, *Analyst*, 2015, **140**, 2656–2663.
32 L. Liu, Z. Jiang, L. Fang, H. Xu, H. Zhang, X. Gu and Y. Wang, *ACS Appl. Mater. Interfaces*, 2017, **9**, 27736–27744.
33 C. Linder, S. G. Rao, A. Le Febvrier, G. Greczynski, R. Sjövall, S. Munktell, P. Eklund and E. M. Björk, *Surf. Coat. Technol.*, 2020, **404**, 126643.
34 M. Thommes, K. Kaneko, A. V. Neimark, J. P. Olivier, F. Rodriguez-Reinoso, J. Rouquerol and K. S. W. Sing, *Pure Appl. Chem.*, 2015, **87**, 1051–1069.
35 A. K. S. Kumar, Y. Zhang, D. Li and R. G. Compton, *Electrochem. Commun.*, 2020, **121**, 106867.
36 K. Y. Foo and B. H. Hameed, *Chem. Eng. J.*, 2010, **156**, 2–10.

© 2026 The Author(s). Published by the Royal Society of Chemistry

Open Access Article. Published on 20 February 2026. Downloaded on 5/25/2026 6:49:37 PM.
This article is licensed under a Creative Commons Attribution-NonCommercial 3.0 Unported Licence.

37 D. I. Cattoni, O. Chara, S. B. Kaufman and F. L. González Flecha, *PLoS One*, 2015, **10**, e0146043.
38 X. Wang, C. Dai, Y. Wu, Y. Liu and D. Wei, *Nat. Protoc.*, 2023, **18**, 2313–2348.
39 B. D. Wilson and H. T. Soh, *Trends Biochem. Sci.*, 2020, **45**, 639–649.
40 S. H. Ha and J. E. Ferrell Jr, *Science*, 2016, **352**, 990–993.
41 O. S. Fedorova, D. B. Lim and V. M. Berdnikov, *React. Kinet. Catal. Lett.*, 1978, **8**, 371–375.
42 T. Yang, R. Xiao, F. Lu, X. Ke, M. Wang and K. Wang, *New J. Chem.*, 2025, **49**, 6674–6683.
43 K. Charoenkitamorn, P. T. Tue, K. Kawai, O. Chailapakul and Y. Takamura, *Sensors*, 2018, **18**, 444.
44 A. J. Bard, L. R. Faulkner and H. S. White, *Electrochemical methods: fundamentals and applications*, John Wiley & Sons, 2022.
45 J. Wu, J. Suls and W. Sansen, *Electrochem. Commun.*, 2000, **2**, 90–93.
46 J. Shen, P. T. Griffiths, S. J. Campbell, B. Utinger, M. Kalberer and S. E. Paulson, *Sci. Rep.*, 2021, **11**, 7417.
47 X.-X. Xie, Y.-C. Yang, B.-H. Dou, Z.-F. Li and G. Li, *Coord. Chem. Rev.*, 2020, **403**, 213100.
48 L.-Y. Zhu, Y.-C. Li, J. Liu, J. He, L.-Y. Wang and J.-D. Lei, *Pet. Sci.*, 2022, **19**, 1371–1381.
49 A. Javed, I. Strauss, H. Bunzen, J. Caro and M. Tiemann, *Nanomaterials*, 2020, **10**, 1263.
50 L. Liu, W. Chen and Y. Li, *J. Membr. Sci.*, 2016, **504**, 1–9.
51 X. Liu, H. Gao, J. E. Ward, X. Liu, B. Yin, T. Fu, J. Chen, D. R. Lovley and J. Yao, *Nature*, 2020, **578**, 550–554.
52 X. Zhao, B. Pattengale, D. Fan, Z. Zou, Y. Zhao, J. Du, J. Huang and C. Xu, *ACS Energy Lett.*, 2018, **3**, 2520–2526.
53 L. Sondermann, W. Jiang, M. Shviro, A. Spieß, D. Woschko, L. Rademacher and C. Janiak, *Molecules*, 2022, **27**, 1241.
54 S. Murugaiyan, M. S. Shabanur Matada, G. P. Kuppuswamy, S. Velappa Jayaraman, C. Di Natale and Y. Sivalingam, *ACS Appl. Nano Mater.*, 2025, **8**, 20164–20176.
55 M. S. Shabanur Matada, V. Nutalapati, S. Velappa Jayaraman and Y. Sivalingam, *ACS Appl. Mater. Interfaces*, 2025, **17**, 20806–20819.
56 W.-Q. Wang, H. Xie, F. Cheng, T. Zou, K.-Q. Xu, A. A. Dubale, W.-H. Zhang, N. Xu, X.-L. Yang and M.-H. Xie, *Chem. Eng. J.*, 2025, 169190.
57 X.-X. Dong, T.-L. Chen, X.-J. Kong, S. Wu, F.-F. Kong and Q. Xiao, *Anal. Methods*, 2024, **16**, 704–708.
58 S. Wang, P. Li, J. Wang, J. Gong, H. Lu, X. Wang, Q. Wang and P. Xue, *Molecules*, 2024, **29**, 2413.
59 M. Mai, B. Liao, Y. Liao, D. Lin and X. Ma, *J. Appl. Electrochem.*, 2023, **53**, 2411–2419.
60 A. Hankin, F. E. Bedoya-Lora, J. C. Alexander, A. Regoutz and G. H. Kelsall, *J. Mater. Chem. A*, 2019, **7**, 26162–26176.
61 G. E. M. Schukraft, B. Moss, A. G. Kafizas and C. Petit, *ACS Appl. Mater. Interfaces*, 2022, **14**, 19342–19352.
62 A. Michaelides, P. Hu, M.-H. Lee, A. Alavi and D. A. King, *Phys. Rev. Lett.*, 2003, **90**, 246103.
63 T.-C. Leung, C. L. Kao, W. S. Su, Y. J. Feng and C. T. Chan, *Phys. Rev. B: Condens. Matter Mater. Phys.*, 2003, **68**, 195408.